Supporting Information

Highly Efficient Circulating Tumor Cell Isolation from Whole Blood and Label-free Enumeration Using Polymer-Based Microfluidics with an Integrated Conductivity Sensor

*André A. Adams, Paul I. Okagbare, Juan Feng, Matuesz L. Hupert, Don Patterson, Jost Göttert, Robin L. McCarley, Dimitris Nikitopoulos, Michael C. Murphy and Steven A. Soper**

Department of Chemistry, Louisiana State University, Baton Rouge, LA 70803
Department of Mechanical Engineering, Louisiana State University, Baton Rouge, LA 70803
Center for Advanced Microstructures and Devices, Louisiana State University, Baton Rouge, LA 70803
E-mail: chsope@lsu.edu, Telephone: +1 (225) 578-1527, Fax: +1 (225) 578-3458

HTMSU fabrication. The HTMSU was manufactured via micro-replication from a metal master. Microstructures were milled onto the surface of a brass plate with a high-precision micromilling machine (KERN MMP 2522, KERN Micro- und Feinwerktechnik GmbH & Co.KG; Germany) following our previously published procedures.[1] The micromilling machine was fitted with a laser measuring system (LaserControl NT, Blum-Novotest GmbH, Germany) for automatic determination of tool length and radius, and an optical microscope (Zoom 6000, Navitar, Inc. Rochester, NY) for monitoring the milling process. Micromilling was carried out at 40,000 rpm. Feed rates were dependent on the size of the milling tool and were typically in the range of 200 mm/min for a 500 μm milling bit, 100 – 150 mm/min for the 200 μm bit, 50 – 75 mm/min for the 100 μm bit and 10-20 mm/min for a 50 μm bit. A typical milling cycle consisted of a pre-cut of the entire surface with a 500 μm milling bit to ensure parallelism between both faces of the brass plate and uniform height of the final milled microstructures over the entire pattern, a rough milling of the microstructures using either a 500 or 200 μm milling bit, and a finishing cut with a smaller diameter milling bit. In the final step of mold master fabrication, burrs were removed by mechanical polishing. Polishing was performed by hand on a 3 μm grain-size polishing paper (Fibrmet Discs - PSA, Buehler, Lake Bluff, IL) followed by polishing on a polypropylene cloth (Engis, Wheeling, IL) with a 1 μm diamond suspension (Metadi Diamond Suspension, Buehler).

Three identical HTMSUs were patterned onto the master enabling production of the units in triplicate during each hot embossing step. In order to accommodate the Pt electrodes used for the conductivity sensor and the inlet/outlet capillaries, the HTMSU was designed with multilevel features.[1] The depth of the HTMSU detection zone was tapered to 80 μm from the 150 μm used in the cell selection beds and throughout the inlet region. The detection channel width was tapered from 100 μm to 50 μm over a 2.5 mm region beginning at the converged outlet and terminating 2.5 mm from the conductivity electrodes scaled for specific detection of CTCs. In the cell selection bed, channel widths (35 μm) that closely matched the average target cell diameter were used to increase the probability of cell-immobilized antibody encounters. To reduce the pressure drops when the device was operated at high volumetric flow rates, the HTMSU was designed with deep (150 μm), high-aspect ratio channels.

Prior to embossing and assembly, PMMA substrates and cover plates were cleaned with reagent grade isopropyl alcohol, IPA (Sigma-Aldrich, St. Louis, MO), rinsed with 18 MΩ nanopure H_2O obtained from a water purification system (D8991, Barnstead/Thermolyne, Dubuque, IA), sonicated for 30 min, rinsed with IPA again and air dried. Hot embossing was performed with a Jenoptik Microtechnik HEX02 (Jena, Germany). For embossing PMMA, the substrate was heated to 140°C and a pressure of 20 kN was applied for 630 s. After the HTMSUs were hot embossed, they were cooled to room temperature and cleaned with IPA.

Regio-specific ultraviolet (UV) modification of the PMMA substrate and cover plate was performed through an aluminum photomask to facilitate the formation of the carboxylated scaffold for directed antibody tethering exclusively within the cell selection beds of the HTMSU. Before final assembly via thermal fusion bonding, the PMMA cover plate and substrate were locally irradiated at 254 nm with 15 mW cm^{-2} fluence for 10 min using a UV exposure station (ABM, Inc., San Jose, CA). Additionally, into the inlet/outlet ports of the device were inserted 237 µm OD and 150 µm ID polyimide-coated fused silica capillaries and the Pt electrodes fabricated with the required gap (see Materials and Methods). After thermally annealing the cover plate to the substrate, a thin film of epoxy resin was applied to the capillary-device interfaces to prevent leaks.

Following UV modification of PMMA, the physicochemical properties of the surface were effectively altered resulting in a moderate reduction of the glass transition temperature (T_g) at the cover plate-substrate interface. The resulting T_g allowed for efficient thermal fusion bonding at 101°C rather than the 106°C T_g of pristine PMMA,[2,3] which could reduce potential thermal deformation of the high-aspect ratio microfeatures. Thermal fusion bonding was carried out in a gas chromatographic (GC) oven (Varian 3400, Palo Alto, CA) using the PMMA cover plate and the open-faced, hot embossed PMMA substrate. The substrate and cover plate were aligned and clamped together between two borosilicate glass plates and the assembly placed into the temperature programmable oven of the GC, where the temperature was increased from 50°C to 101°C at a rate of 20°C/min. The temperature was held at 101°C for 15 min.

Conductivity detection electronics. To measure conductance changes in the CTC releasing buffer of the HTMSU induced by single CTCs, a specially-designed circuit was developed (see Figure S1). To reduce the effects of parasitic capacitance, $C_{p,}$ due to wiring and the electrode configuration, a synthetic inductor, L, of 132 mH was designed using a gyrator circuit. Gyrators, for a given bandwidth, allow the creation of high Q inductors from RC components. This inductance was placed in parallel with C_p and the sine frequency varied to locate the resonance peak of the voltage across L and C_p. Once this resonance point was found, the voltage across the sample cell was directly sensitive to changes in G_s (solution conductance). A target frequency of 40 kHz was chosen to minimize the impedance due to C_d (double layer capacitance) and hold the inductance to a reasonable value. This signal was fed to a transconductance amplifier, $G_{1,}$ which converted the voltage sinusoid into a current. The gain of G_1 was 10 μA/volt. A current source was needed to drive the sample cell because a voltage source, with its low output impedance, would reduce the circuit's Q. The current was set to ±5 μA for the experiments. The required resonance frequency (*f*) could be approximated by the standard parallel resonance equation;

$$f = {}^{1}\!/_{2\pi}\,(LC_p)^{1/2} \quad \text{(S1)}$$

The voltage across the sample cell was fed to an Analog Devices AD630 synchronous modulator/demodulator (Norwood, MA) that was configured as a phase sensitive detector. The reference input of the AD630 was driven from a phase-delayed sine wave oscillator output. This phase adjustment was needed to compensate for phase lags in the detected sample voltage. The sample voltage was fed to a low pass filter with a cutoff frequency of 180 Hz. The filter produced an average dc signal that was sent to a differencing amplifier, A_1. The difference amplifier served to null the output to zero volts while measuring G_S. A high gain amplifier, $A_{2,}$ could amplify small changes in G_S without saturating the voltage produced by the releasing buffer itself. A National Instruments PCI6071E, 12 bit A/D acquisition card (Austin, TX) was used to convert the analog signal to a 12 bit digital signal.

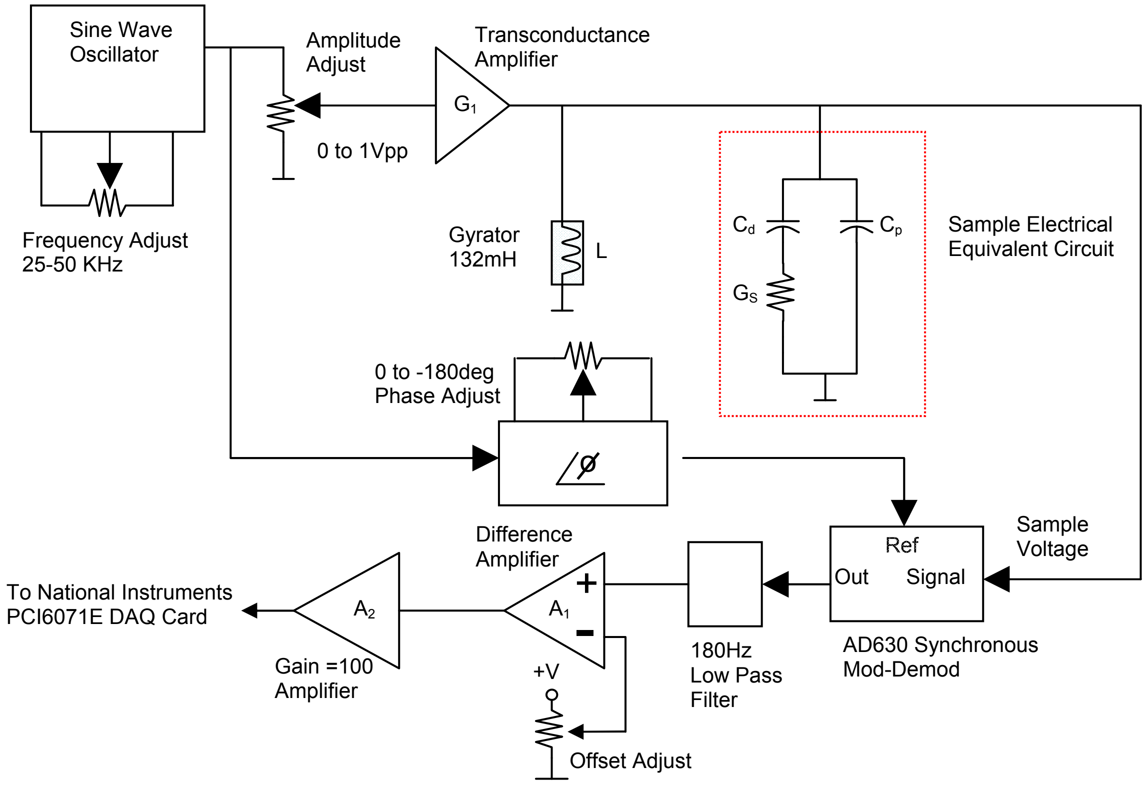

Figure S1. Circuit diagram for the conductivity sensor.

Pressure drop in a microchannel with blood flow. The volume flow of blood (Q) in an enclosed microchannel can be calculated from a modified version of Poiseulle flow using Equation S2;

$$Q = \frac{\pi d_h^4}{128\eta} \cdot \frac{dP}{dX} \cdot F(\varepsilon) \quad \text{(S2)}$$

where d_h is the hydraulic diameter of the microchannel (see equation S8 below), η is the solution viscosity, dP/dX is the pressure drop (see below) and $F(\varepsilon)$ is calculated from;

$$F(\varepsilon) = 1 - \frac{16}{7}\varepsilon^{1/2} + \frac{4}{3}\varepsilon - \frac{1}{21}\varepsilon^4 \quad \text{(S3)}$$

The term $F(\varepsilon)$ accounts for the viscosity-dependent hematocrit level of whole blood with ε determined from Equation S4;

$$\varepsilon = \frac{4\tau_y}{D} \cdot \left(-\frac{dP}{dX}\right)^{-1} \quad \text{(S4)}$$

where τ_y is the yield stress and is related to the blood hematocrit level (*H*) using;

$$\tau_y = -0.1 \cdot (0.625H)^3 \quad \text{(S5)}$$

From equation S2, the pressure drop (ΔP) in a channel of length *L* can be calculated from;

$$\Delta P = \frac{128\eta L}{\pi d^4 F(\varepsilon)} Q \quad \text{(S6)}$$

Flow dynamics in sinusoidally-shaped microchannels with high transport velocities (U). The critical non-dimensional parameter used in microfluidics to characterize the flow stability is the Reynolds number, which is given by;

$$\mathrm{Re} = \frac{\rho U d_h}{\mu} \quad \text{(S7)}$$

where ρ is the fluid density, *U* is the fluid velocity, μ the viscosity of the fluid, and d_h is the hydraulic diameter of the channel, given by;

$$d_h = \frac{4wh}{2(w+h)} = \frac{2wh}{w+h} \quad \text{(S8)}$$

Our experiments were run at flow velocities ranging from 1 mm s^{-1} to10 mm s^{-1}. Using the parameters delineated in Table S1, the Reynolds numbers for the flows ranged between 0.0159 at 1 mm s^{-1} to 0.159 at 10 mm s^{-1}. These values are well within the laminar flow regime (R > 2000 for turbulent flow).

Table S1. Parameters for sinusoidally-shaped microfluidic channels using the viscosity and density of water as a representative model.

Parameter	**Symbol**	**Value**
Channel width	W	35 μm
Channel depth	H	150 μm
Hydraulic diameter	d_h	142 μm
Sinusoid amplitude	A	48 μm
Sinusoid period		376 μm
Viscosity	μ	8.9 X 10^{-4} Pa s
Density	ρ	997.04 kg/m^3

To better understand flow in curved channels, a second non-dimensional parameter, the Dean number, needs to be calculated as well. This arises from early work on flow in curved channels by Dean.[4] The Dean number is given by;

$$\mathrm{De} = \sqrt{\frac{d_h}{R_c}}\frac{\rho V d_h}{\mu} = \sqrt{\frac{d_h}{R_c}}\mathrm{Re} \quad \text{(S9)}$$

where d_h is the hydraulic diameter of the channel and R_c is the radius of curvature of the bend. Dean identified a threshold Dean number of 35.92 for the onset of flow instability. At lower Dean numbers, the flow is characterized as "curved channel Poiseulle flow" (CCPF).[4] In CCPF, the velocity is entirely streamwise with a parabolic profile similar to plane channel flow except that the maximum velocity is shifted toward the concave or outer wall in a bend making the velocity distribution asymmetric.

Calculation of the Dean number for the sinusoidal channel requires evaluation of the radius of curvature, which varies along the sinusoid. To do this a parametric representation of the sinusoid can be used;

$$\begin{aligned} x(t) &= B \cdot t \\ y(t) &= A \sin t \end{aligned} \quad \text{(S10)}$$

The curvature for a two-dimensional parametric representation is then;

$$\kappa(x,y,t) = \frac{\frac{dx}{dt}\frac{d^2y}{dt^2} - \frac{dy}{dt}\frac{d^2x}{dt^2}}{\left(\left(\frac{dx}{dt}\right)^2 + \left(\frac{dy}{dt}\right)^2\right)^{\frac{3}{2}}} \quad \text{(S11)}$$

The radius of curvature is the inverse of the curvature calculated from;

$$R_c = \frac{1}{\left|\kappa(x,y,t)\right|} \quad \text{(S12)}$$

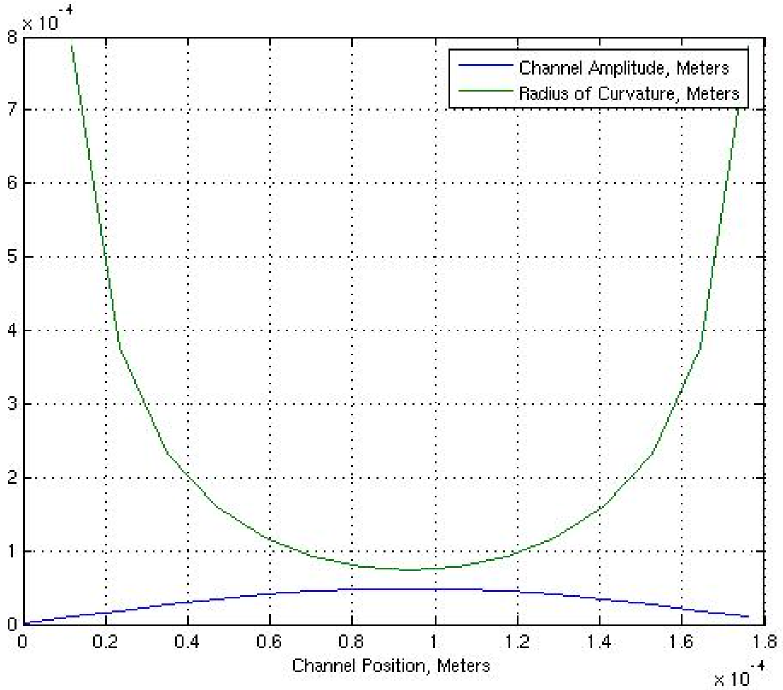

Figure S2. The lower curve is the profile of the sinusoidal channel and the upper curve the radius of curvature.

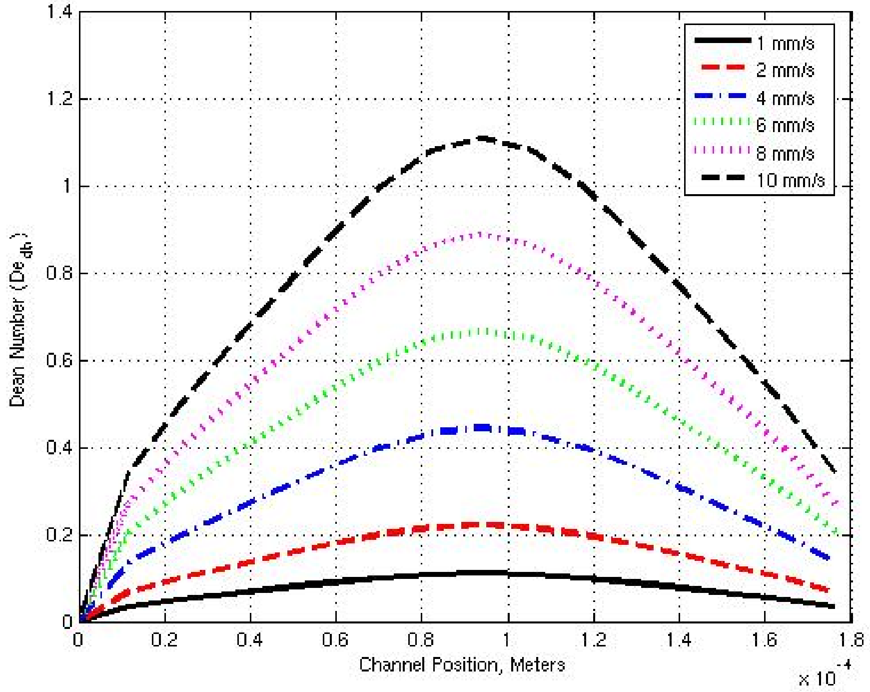

Figure S3. Dean numbers based on the hydraulic diameter calculated using the radius of curvature from Figure S2 and Re calculated for the range of velocities used in these experiments.

Using the parameters in Table S1 to calculate a representative radius of curvature produced the result shown in Figure S2. The radius of curvature goes to infinity when $t = (0, \pi, 2\pi)$ and is a minimum at $t = (\pi/2, 3\pi/2,)$. Using the radius of curvature, the Dean number was calculated for the sinusoidal channel and flow velocities ranging from 1 mm s^{-1} to 10 mm s^{-1} (see Figure S3). The maximum in the Dean number was ~1.1, much less than the threshold for the onset of Dean instabilities. The approximation of the hydraulic diameter introduces errors for aspect ratios greater than 3, so the Dean number was recalculated using the width of the channel, w, as the characteristic dimension. The Dean number based on the width is less than the Dean number estimated using the hydraulic diameter (see Figure S4), so there is no change in the flow as a consequence. The flow in our sinusoidal channels was CCPF, laminar with the maximum flow velocity offset towards the concave side of the curve. Additional pressure drops were negligible although there were still bend loss effects.

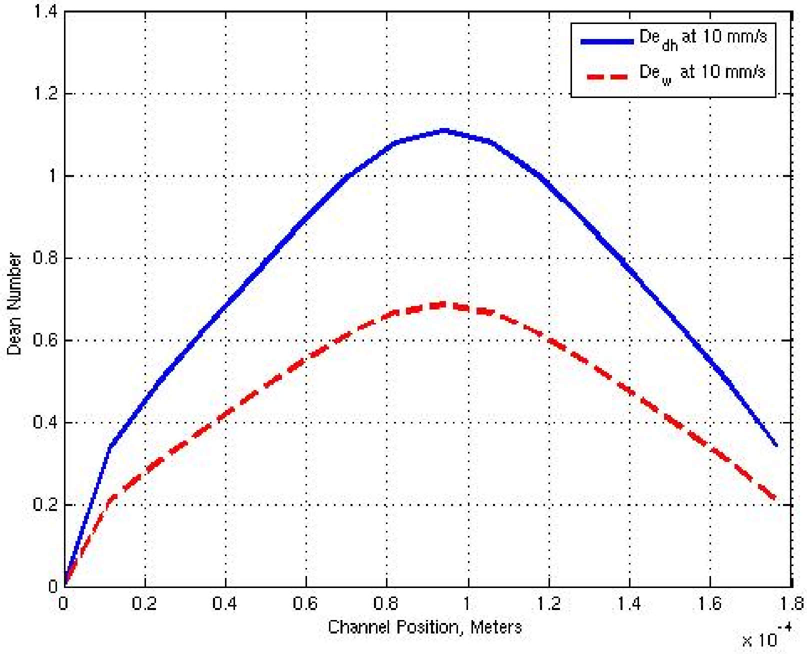

Figure S4. Dean number based on the hydraulic diameter compared to the Dean number based on the channel width at 10 mm/s. The hydraulic diameter value is larger and consequently a more conservative estimate.

Modeling cell capture data as a function of the cell translational velocity (U). To explain the experimental data in terms of capture efficiency versus the linear flow rate, the data for the 35 μm wide sinusoidally-shaped channels was modeled by adopting the 2-state model developed by Chang and Hammer, with the assumption that transport was dominated by convection (*i.e.*, Pe >> 1, where Pe is the Peclet number and represents the ratio of convective to diffusive mass transport).[5] In this model, the rate of capture of cells at a surface containing immobilized recognition elements depends on the encounter rate and the reaction time. The rate of capture per ligand/receptor pair (k_f, s^{-1}) can be calculated with Equation S13;

$$k_f = k_o P \qquad \text{(S13)}$$

where k_o is the encounter rate and describes the rate of transport of cells to the wall where the antibodies are immobilized and P is the probability of a reaction occurring between the cell ligand (*i.e.,* EpCAM) and surface receptor. For Pe >> 1, as in the current experiments, k_f is primarily reaction limited and is calculated using Equation S14;

$$k_f = \pi D Nu P \quad \text{(S14)}$$

where *D* is the cell diffusion coefficient and *Nu* is the Nusselt number, which describes the flux of antigens to immobilized antibodies and can be approximated from $2Pe/\pi$ for *Pe* >> 1. *P* is estimated from Equation S15;

$$P = {}^{\Lambda\delta}/_{(1 + \Lambda\delta)} \quad \text{(S15)}$$

where δ is the dimensionless Damköhler number ($a^2 k_{in}/D$; k_{in} = intrinsic EpCAM:anti-EpCAM reaction rate; *a* is the encounter radius) and Λ is the dimensionless encounter time and is calculated from $\tau/(a^2/D)$, where $\tau = 8a/(3U\pi)$. A plot of k_o, *P*, and k_f versus the cell slip velocity, where the slip velocity is ~0.47*U*, are depicted in Figure S5.

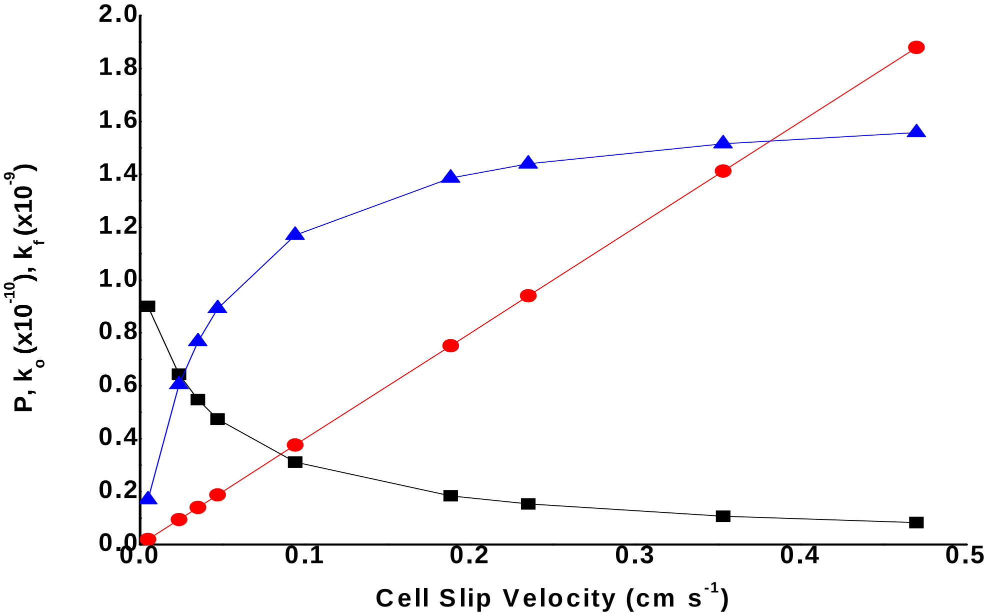

Figure S5. Plot of *P* (black rectangles), k_o (red circles) and k_f (blue triangles) as a function of the input cell slip velocity into a fluidic channel of dimensions 35 µm x 150 µm.

The experimental data (% of input cells bound to the channel wall) can be used to calculate the rate of adsorption, k_{ads}, from;

$$k_{ads} = \frac{-U}{L} \ln\left[1 - \%bound\right] \quad \text{(S16)}$$

where L is the length of the capture channel and U is the translational velocity of the cells within the fluidic channel. Finally, k_{ads} is related to k_f through the relationship;

$$k_f = {k_{ads}}/{C_\infty N_r} \quad \text{(S17)}$$

where C_∞ is the cell surface antigen density and N_r is the number of antibodies in the encounter area ($2\pi a^2$). Therefore, a plot of U versus k_{ads}, which is obtained from the experimental data, can be fit to Equation S14 with one adjustable parameter, k_{in}, that is used for the estimation of P.

Adhesion strength of EpCAM:anti-EpCAM antibody complex on a surface. The adhesion force (F_A) between the cell and the antibody-decorated surface can be determined from the bond strength between a single antigen:antibody complex (f_c), the cell contact area with the PMMA surface (A_c) and the number of receptors poised on the PMMA surface within the contact area of the cell (C_s) from:

$$F_A = f_c \times A_c \times C_s \quad \text{(S18)}$$

If the cell is assumed to be a non-deformable object upon adhesion to the capture surface, the contact area can be calculated using Equation S19;[6]

$$A_c = \pi r^2 \sin\left(cos^{-1}\left(r - h' + {h}/{r}\right)\right) \quad \text{(S19)}$$

where r is the cell radius and h and h' represent the characteristic cell separation distances from the surface upon binding. Using h and h' as 100 Å and 400 Å, respectively,[7] the calculated contact area was determined to be 16.6 μm^2 for the MCF-7 cells. If the cell is assumed to flatten and elongate after contact, as observed experimentally (see Figure S6), the resulting contact area A_c is 456 μm$^{2.8}$

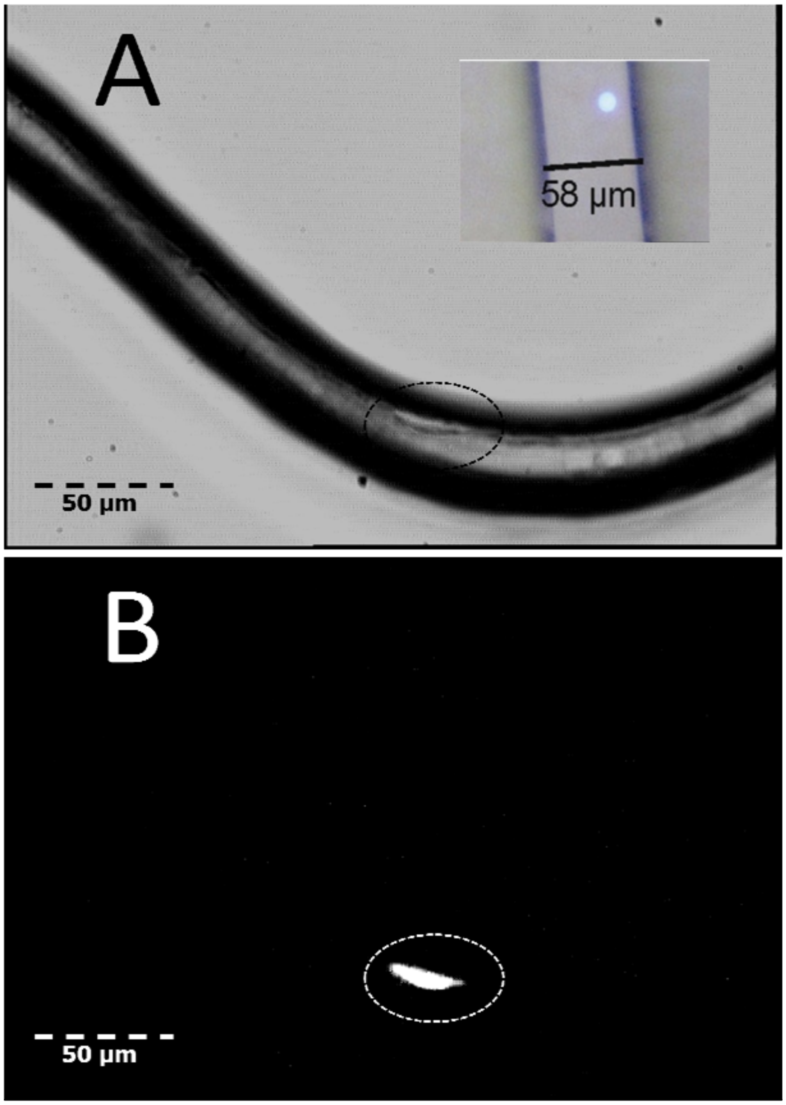

Figure S6. Brightfield and fluorescence micrographs showing monoclonal antibody captured CTCs in a PMMA microchannel. (A) Brightfield micrographs taken at 40× magnification and (B) the corresponding fluorescence micrographs verifying the captured cell is the fluorescently labeled CTC. The inset shown in Panel (A) is a fluorescently-stained MCF-7 cell in a PMMA channel that was not decorated with anti-EpCAM antibodies indicating the spherical shape of these cells.

The single EpCAM:anti-EpCAM antibody adhesion force was estimated using the formalism by Bell,[9] who developed the following expression for deriving the critical force required to break a single bond (Equation S20);

$$f_c = {}^{kT}\!/_{r_o}\, \alpha_c \quad \text{(S20)}$$

where k is Boltzman's constant, T is the absolute temperature, r_o is the separation distance between receptors at the minimum breaking force and $\alpha_c = KC_s$ (K = EpCAM:anti-EpCAM equilibrium constant). Using values from Table S2 and T = 298K, a value of 6.7 x 10^{-6} dynes was calculated for f_c. The same result was found using Dembo's binding affinity model.[8,10,11]

Table S2. Literature values for the complex between EpCAM and its monoclonal antibody. Additional properties of the EpCAM:anti-EpCAM thermodynamic properties can be found in Ref. 19.

Parameter	**Description**	**Value**	**Reference**
a	Encounter radius	5 nm	5
k_{in}	Forward rate constant for EpCAM - anti-EpCAM binding	0.99 x 10^{5} s^{-1}	12
r	MCF-7 average cell radius	12 μm	13
H	Blood hematocrit level	0.4	14
L	Cell selection bed length	35 mm	
d	Microchannel hydraulic number	56 μm	15
D	MCF-7 cell diffusion coefficient	10^{-10} cm^{2} s^{-1}	16
η	Viscosity of blood (H = 0.4)	4.8 cP	14
C_∞	Cell surface density of EpCAM - calculated from the average surface area of MCF-7 cells and the expression level of EpCAM	282 μm^{-2}	17
N	Expression level of EpCAM in MCF-7 cells	5.1 x 10^{5}	17
K	EpCAM:anti-EpCAM equilibrium constant	3.3 x 10^{8} M^{-1}	12
r_o	Separation distance between receptors at min. breaking force	0.5 nm	5
N_L	Substratum anti-EpCAM density on UV-modified PMMA	2.3 x 10^{11} cm^{-2}	18

References

(1) Hupert, M. L.; Guy, W. J.; Llopis, S. D.; Shadpour, H.; Rani, S.; Nikitopoulos, D. E.; Soper, S. A. *Microfluid. Nanofluid.* **2007**, *3*, 1-11.

(2) Henry, A. C.; Tutt, T. J.; Galloway, M.; Davidson, Y. Y.; McWhorter, C. S.; Soper, S. A.; McCarley, R. L. *Anal. Chem.* **2000**, *72*, 5331-5337.

(3) Galloway, M.; Stryjewski, W.; Henry, A.; Ford, S. M.; Llopis, S.; McCarley, R. L.; Soper, S. A. *Anal. Chem.* **2002**, *74*, 2407-2415.

(4) Ligrani, P. M.; Niver, R. D. *Physics of Fluids* **1998**, *31*, 3605-3617.

(5) Chang, K. C.; Hammer, D. A. *Biophys. J.* **1999**, *76*, 1280-1292.

(6) Cozens-Robert, C.; Quinn, J. A.; Lauffenburer, D. A. *Biophys. J.* **1990**, *58*, 107-125.

(7) Clausen, J. *Immunochemical techniques for the identification and estimation of macromolecules, In Laboratory Techniques in Biochemistry and Molecular Biology*, 1981; Vol. 1.

(8) Feng, J.; Soper, S. A.; McCarley, R. L.; Murphy, M. C. In *Lasers in Surgery XIV* Proceedings of the SPIE: San Jose, CA, 2004; Vol. 5312, p 278-293.

(9) Bell, G. I. *Science (Washington, DC, United States)* **1978**, *200*, 618-27.

(10) Dembo, M.; Torney, D. C.; Saxman, K.; Hammer, D. *Proceedings of the Royal Society of London Series B-Biological Sciences* **1988**, *234*, 55-83.

(11) Kuo, S. C.; Lauffenburger, D. A. *Biophys. J.* **1993**, *65*, 2191-2200.

(12) Willuda, J.; Honegger, A.; Waibel, R.; Schubiger, P. A.; Stahel, R.; Zangemeister-Wittke, U.; Pluckthun, A. *Cancer Res.* **1999**, *59*, 5758-5767.

(13) Depasquale, J. A.; Samsonoff, W. A.; Gierthy, J. F. *J. Cell Sci.* **1994**, *107*, 1241-1254.

(14) Kameneva, M. V.; Watach, M. J.; Borovetz, H. S. *Clin. Hemorheol. Microcirc.* **1999**, *21*, 357-363.

(15) Chein, R. Y.; Yang, Y. C.; Lin, Y. S. *Electrophoresis* **2006**, *27*, 640-649.

(16) Dieterich, P.; Klages, R.; Preuss, R.; Schwab, A. *Proc. Natl. Acad. Sci. U. S. A.* **2008**, *105*, 459-63.

(17) Rao, C. G.; Chianese, D.; Doyle, G. V.; Miller, M. C.; Russell, T.; Sanders, R. A.; Terstappen, L. W. M. M. *Int. J. Oncol.* **2005**, *27*, 49-57.

(18) McCarley, R. L.; Vaidya, B.; Wei, S.; Smith, A. F.; Patel, A. B.; Feng, J.; Murphy, M. C.; Soper, S. A. *J. Am. Chem. Soc.* **2005**, *127*, 842-843.

(19) Meng, S., et al., *Proc. Natl. Acad. Sci. U.S.A.* **2004**, *101*, 9293-9298.